metals

MDPI

Article

Microstructure and Physico-Mechanical Properties of Biocompatible Titanium Alloy Ti-39Nb-7Zr after Rotary Forging

Anatoly Illarionov [1], Galymzhan Mukanov [1,*], Stepan Stepanov [1], Viktor Kuznetsov [1], Roman Karelin [2], Vladimir Andreev [2], Vladimir Yusupov [2] and Andrei Korelin [1]

[1] Institute of New Materials and Technologies, Ural Federal University Named after the First President of Russia B.N. Yeltsin, 19 Mira Str., 620002 Yekaterinburg, Russia; a.g.illarionov@urfu.ru (A.I.); s.i.stepanov@urfu.ru (S.S.); v.p.kuznetsov@urfu.ru (V.K.); a.v.korelin@urfu.ru (A.K.)

[2] Baikov Institute of Metallurgy and Materials Science, Leninsky Prospekt, 49, 119334 Moscow, Russia; r.karelin@imet.ac.ru (R.K.); vandreev@imet.ac.ru (V.A.); vsyusupov@mail.ru (V.Y.)

* Correspondence: g.zh.mukanov@urfu.ru; Tel.: +7-912-692-4334

Abstract: The evolution of microstructure, phase composition and physico-mechanical properties of the biocompatible Ti-39Nb-7Zr alloy (wt.%) after severe plastic deformation by rotary forging (RF) was studied using various methods including light optical microscopy, scanning and transmission electron microscopies, X-ray diffraction, microindentation, tensile testing and investigation of thermophysical properties during continuous heating. The hot-rolled Ti-39Nb-7Zr with initial single β-phase structure is subjected to multi-pass RF at 450 °C with an accumulated degree of true deformation of 1.2, resulting in the formation of a fibrous β-grain structure with imperfect 500 nm subgrains characterized by an increased dislocation density. Additionally, nano-sized α-precipitates formed in the body and along the β-grain boundaries. These structural changes resulted in an increase in microhardness from 215 HV to 280 HV and contact modulus of elasticity from 70 GPa to 76 GPa. The combination of strength and ductility of Ti-39Nb-7Zr after RF approaches that of the widely used Ti-6Al-4V ELI alloy in medicine, however, Ti-39Nb-7Zr does not contain elements with limited biocompatibility and has a modulus of elasticity 1.5 times lower than Ti-6Al-4V ELI. The temperature dependences of physical properties (elastic modulus, heat capacity, thermal diffusivity) of the Ti-39Nb-7Zr alloy after RF are considered and sufficient thermal stability of the alloy up to 450 °C is demonstrated.

Keywords: low-modulus β-Ti alloy; rotary forging; biocompatibility; UFG; TNZ; microstructure; mechanical properties; phase composition

Citation: Illarionov, A.; Mukanov, G.; Stepanov, S.; Kuznetsov, V.; Karelin, R.; Andreev, V.; Yusupov, V.; Korelin, A. Microstructure and Physico-Mechanical Properties of Biocompatible Titanium Alloy Ti-39Nb-7Zr after Rotary Forging. *Metals* **2024**, *14*, 497. https://doi.org/10.3390/met14050497

Academic Editor: Wenlong Xiao

Received: 22 March 2024
Revised: 21 April 2024
Accepted: 22 April 2024
Published: 24 April 2024

1. Introduction

Several types of titanium alloys (α-, α+β-, β-) are widely used in medicine due to their excellent biocompatibility, low density and high specific strength [1–5]. Commercially pure (CP) titanium with an Hexagonal Close-Packed (HCP) α-solid solution structure and two-phase (α+β)-alloy Ti-6Al-4V ELI [6] are among the most commonly employed materials for medical implant manufacturing. The microstructure of Ti-6Al-4V ELI comprises a minor fraction of β-solid solution (2–10%) with BCC lattice along with the α-phase (90–98%). However, these alloys have several drawbacks in manufacturing implants for orthopedic applications: (1) high modulus of elasticity (100–112 GPa) characteristic of the predominant α-phase structure, which promotes the atrophy of the bone tissue with a lower modulus of (1–30 GPa) adjacent to the implant; (2) low strength characteristics of CP titanium after conventional processing [1], which requires the increased implant sizes and leads to an excessive load on the patient's organism; (3) the presence of Al and V in the Ti-6Al-4V alloy imposes limitations on the safe usage period of implants, as they can induce undesirable side effects upon dissolution in the patient's body [7] (e.g., allergic reactions, toxicity, mutagenicity).

To address these shortcomings, extensive research on the development of β-solid solution titanium alloys has been conducted in recent decades [2,3,8–13]. The titanium β-alloys are primarily alloyed with biocompatible β-stabilizers (Nb, Mo, Ta) and neutral strengtheners (Zr, Sn) for orthopedic use [7]. Based on several parameters (abundance in nature, density, modulus of elasticity, atomic size, melting temperature [14,15]), Nb and Zr can be considered the most promising alloying elements for titanium β-alloys [16,17]. Despite a number of advantages of β-titanium alloys compared to CP-Ti and two-phase (α+β)-alloys, such as lower modulus of elasticity and absence of toxic alloying elements, these alloys have their own challenges to overcome: higher cost and density, relatively low strength (hardness) and wear resistance of the β-solid solution-based alloys.

One approach to enhance the strength of biocompatible β-titanium alloys is through strain hardening combined with grain refinement, achieved by employing severe plastic deformation (SPD) methods [18–21]. At the same time, widely used methods of severe plastic deformation, such as high-pressure torsion (HPT), equal-channel angular pressing (ECAP), and multidirectional isothermal forging (MIF), are associated with several significant drawbacks. The main disadvantages of HPT are the small sizes of the processed workpieces and the low durability of the tooling resulting from high loads [22]. MIF has a limitation on the degree of single deformation path due to the loss of workpiece stability at high compression strains. MIF is characterized by the inhomogeneity of deformation and structure across the workpiece cross-section, which requires a large number of processing cycles to be avoided [22]. The drawbacks of ECAP include the relatively small size of the obtained semifinished products, the inhomogeneous structure of the final material, and significant wear of the tooling due to high loads. Currently, traditional metal forming processes are being developed to provide strengthening comparable to SPD methods. Rotary forging (RF) is one such promising metal-forming process [23,24]. RF achieves a compression stress state along the radius of the rotating workpiece by utilizing cyclically converging dies. Its advantages include aspects as follows: (1) the stress distribution in the deformation zone is approaching the scheme of hydrostatic compression, which is most favorable for high technological plasticity at high deformation degrees; (2) semi-finished products with high-quality surfaces and homogeneous microstructure throughout the cross-section can be obtained during RF; (3) high strain rate and impact intensity on the material during RF create conditions for achieving a high-strength state by increasing the density of dislocations and microstructure refinement; (4) reducing the mass of the final product by 35–55% is achievable by increasing the specific strength and fatigue characteristics compared to other traditional metal forming processes (such as rolling, forging, pressing, etc.).

Previous studies devoted to the effect of RF on the microstructure of steels and non-ferrous metals have shown effective refinement of grains and second phases in high-nitrogen steel [25]; improved performance characteristics of the low-carbon steels [26], titanium alpha alloy PT-7M [27], titanium pseudo-beta alloy Ti-15V-3Cr-3Al-3Sn-1Zr-1Mo [28]; and enhancement of such properties as shape memory, corrosion resistance and increased mechanical properties in biocompatible alloys Zr-2.5Nb, nitinols [29,30], and titanium β-alloys Ti-25Nb-15Zr, Ti-15Mo with metastable β-phase [31,32]. However, there is a lack of information in the literature regarding the use of RF for biocompatible alloys based on mechanically stable β-solid solution. Therefore, this study aims to investigate the effect of multi-pass rotary forging on the formation of microstructure and phase composition in the biocompatible β-titanium alloy Ti-39Nb-7Zr.

2. Materials and Methods

The Ti-39Nb-7Zr ingots, obtained via the vacuum arc double electrode remelting process in industrial conditions at PJSC VSMPO-AVISMA Corporation, underwent hot-rolling in the β-field to form a rod with a diameter of 20 mm. The chemical composition of the alloy was selected based on the recommendations outlined in [17] and it is detailed in Table 1.

Table 1. Chemical composition of Ti-39Nb-7Zr in wt.%.

Ti	Nb	Zr	Fe	Ni	Cr
Balance	39.5	7.09	0.031	0.032	0.015

Based on the chemical composition of the investigated alloy, the stability of the β-solid solution to transformations during cooling and deformation was estimated using literature data on molybdenum equivalent ($[Mo]_{eq}$ = %Mo + 0.33%Nb + 0.31%Zr + 1.93%Fe + 1.84%Cr + 2.46%Ni [33]), B_o (binding strength), M_d (energy level of the metallic d-orbital) [34,35], as well as β-transus temperature (β_{tr} = 885 − 8.5Nb − 2Zr [24]) and the martensite start temperature M_S [36,37]. The computed results are summarized in Table 2.

Table 2. Characteristics of the Ti-39Nb-7Zr phase stability.

$[Mo]_{eq}$	β_{tr}, °C	M_S, °C	Bo	Md
15.25	539	−165	2.884	2.464

As can be seen from the computational models, the alloy has a sufficiently lower β_{tr} than CP and Ti-6Al-4V ELI; the M_S lies significantly lower than the room temperature. These data along with the high value of $[Mo]_{eq}$ confirm the high thermal and mechanical stability of the β-solid solution, which was experimentally demonstrated in [38]. Furthermore, the alloy occupies a region in the Bo and Md values diagram [34] where the β-solid solution is predominantly deformed by slip. This characterization indicates the stability of the β-solid solution to quenching and cold deformation processes.

The hot-rolled rod of Ti39Nb7Zr underwent turning to achieve the final diameter d_1 of 18.2 mm, aiming to remove the surface gas-saturated layer formed during the hot rolling. Subsequently, the resulting rod was processed through multi-pass RF to reduce its diameter d_2 to 10.3 mm using a modernized two-die rotary forging machine B2129.01, manufactured by OJSC Pressmash. During the RF process, the rod was constantly pre-heated at a temperature of 450 °C for 20 min (before the 1st pass) and 5 min (between passes). RF totaled 12 passes with a compression of up to 1 mm per pass. The accumulated true strain (ε) during RF was 1.14, there was a total elongation of 3.12, the rod's relative reduction was 68%, and the relative strain by elongation per pass on average was 10%. The schematic diagram of the working space of the RF machine is presented in Figure 1. The photographic image of the rod after forging is shown in Figure 2.

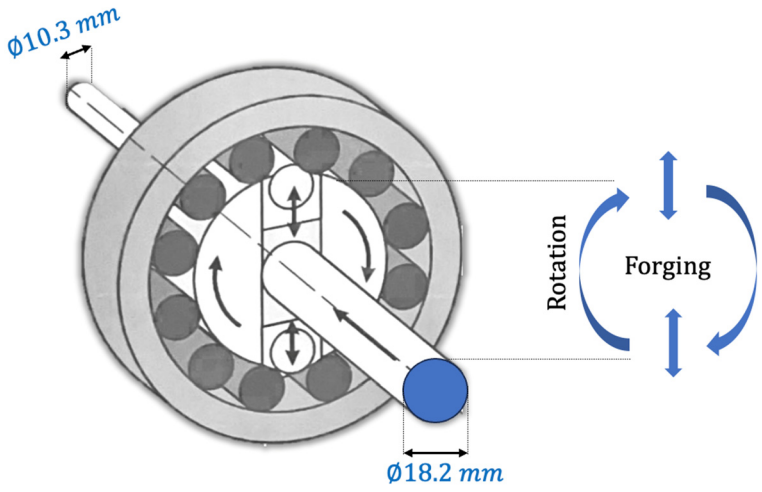

Figure 1. Scheme of the working space of the RF machine.

Figure 2. Photographic image of the Ti39Nb7Zr rod after rotary forging.

The research methods employed in the study included optical microscopy, scanning electron microscopy (SEM) and transmission electron microscopy (TEM), X-ray diffraction phase analysis (XRD), differential scanning calorimetry (DSC), dynamic mechanical analysis (DMA), and Vickers microindentation.

Samples for the metallographic investigation were prepared according to the following procedure:

1. The samples were separated from the rod along the longitudinal section using an electrical discharge machine (EDM) (Ecocut, Bengaluru, India) after deformation processing.
2. The separated samples were hot-mounted using CON conductive resins.
3. The investigated surfaces were ground using abrasive materials of various grit sizes P240, P400, P1000, P1200, and P2500 (with a load of 10 N on the sample for 10 min).
4. Subsequently, the investigated surfaces were polished for 90 min using a suspension composed of 7 parts Col-Si + 3 parts (15%HF + 10%HNO_3 + 75%H_2O), with a load of 25N on the sample.
5. Finally, the polished surfaces were etched using Kroll's reagent (15%HF + 10%HNO_3 + 75%H_2O).

SEM analysis was carried out using a ZEISS CrossBeam AURIGA scanning electron microscope equipped with Oxford Instruments Inca Energy 250 for EDX analysis (Carl Zeiss NTS, Oberkochen, Germany).

TEM analysis was performed using a JEM2100 microscope (Freising, Japan) operating at an accelerating voltage of 200 kV. Foils for TEM investigations were separated using EDM and subsequently thinned on SiC abrasive paper, which was followed by electrolytic thinning using a Struers TenuPol standard A3 reagent.

XRD analysis was conducted using a Bruker D8 Advance (Fremont, CA, USA) equipped with Cu radiation in the 2θ-range of 30–120° with a step size of 0.05°, employing a position-sensitive detector. Full-profile Rietveld refinement of the XRD pattern was carried out using the TOPAS software version 3.0.

Differential thermal analysis (DTA) was performed on specimens with a diameter of 5 mm and height of 1 mm using a heating rate of 20°/min with a Netzsch Jupiter STA 449C (Selb, Germany) up to 700 °C. The dimensions of the reference sample were similar. Platinum crucibles with lids and aluminum oxide attachments were employed to prevent interaction between the sample material and the crucible during the experiments.

The specific heat values of the alloys were calculated based on experimental data obtained from the differential thermal analysis (DTA) of the investigated alloy and a reference material with a known specific heat capacity (sapphire). The specific heat capacity was determined using the following formula [39]:

$$C\_sample = C\_ref * m\_ref * (DTA\_sample - DTA\_blank)/(m\_sample * (DTA\_ref - DTA\_blank)), \quad (1)$$

where C_sample is the specific heat capacity of the sample; C_ref is the specific heat capacity of the reference sample (sapphire); m_ref is the mass of the reference sample; m_sample is the mass of the sample; DTA_sample is the signal of the differential thermocouple (DTA) recorded during sample heating; DTA_blank is the signal of the DTA recorded during heating of the empty system; DTA_ref is the signal of the DTA recorded during heating of the reference sample.

DMA was performed on specimens with a width of 5.5 mm and a thickness of 3.5 mm using a Netzsch DMA 242 C instrument (Selb, Germany). The analysis involved continuous heating up to 600 °C at a rate of 20°/min. Cyclic loading with a frequency of 1 Hz and a maximum load of 5.3 N was applied.

Tensile testing was conducted according to ASTM E8/E8M-21 standards on small-size cylindrical specimens proportional to the standard, with a diameter of 4 mm and a gauge length of 20 mm. The testing was carried out using an electromechanical testing machine Instron 3382 (Instron, High Wycombe, UK), at a crosshead displacement rate of 5 mm/min at room temperature. Vickers hardness (HV) and contact elastic modulus of specimens cut along the rod axis were determined from microindentation tests using a CSM ConScan (CSM Instruments, Peuseux, Switzerland) according to the Oliver–Pharr method. For each specimen, 10 measurements were conducted.

The thermal conductivity of the alloy after RF was determined using the laser flash method (Parker method [40]), implemented on the LFA 457 MicroFlash instrument (NETZSCH, Selb, Germany). Measurements were conducted on three samples during isothermal soakings at the investigated temperatures. The samples, which were parallelepiped in shape, had dimensions of 10 × 10 × 2 mm. During the experiment, the frontal surface of the samples was irradiated with a laser pulse, and the temperature of the rear surface was measured using a fast infrared thermometer. The total measurement time at each temperature did not exceed 15 min. Heating between the temperatures of isothermal holding was carried out at a rate of 3 °C/min in a static argon atmosphere.

3. Results and Discussion

The diffraction pattern and microstructure of the hot-rolled Ti39Nb7Zr rod are represented in Figure 3.

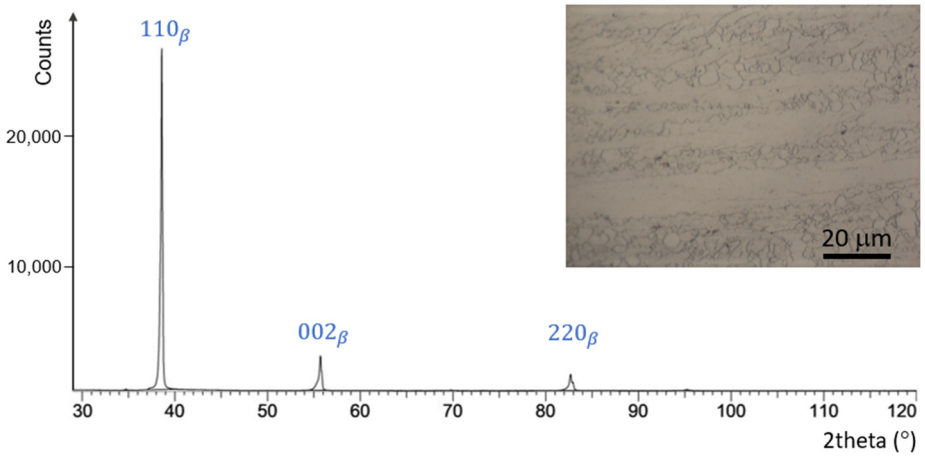

Figure 3. Diffraction pattern obtained from the cross-section and optical microscopy image of the Ti39Nb7Zr hot-rolled rod.

After air-cooling the Ti39Nb7Zr alloy from temperatures of hot rolling in the β-phase region, only three diffraction peaks of the β-solid solution with a BCC lattice are present in the diffraction pattern (Figure 3). Notably, in the diffraction pattern obtained from the cross-section of the rod, the (110) peak exhibits substantially higher intensity compared to other β-phase peaks. Thus, the alloy demonstrates a single-phase β-state with a predominant <110>-fiber orientation along the rolling axis, which is the typical texture for the rolling of BCC alloys [41]. The calculated β-phase lattice spacing of 0.3296 nm is significantly higher than the extrapolated value for pure titanium (0.3282 nm [42]), this is attributed to the larger atomic size of the alloying elements (142.9 pm–Nb, 155.36 pm–Zr) compared to the titanium atom in the BCC lattice (142.11 pm) [43].

The microstructure analysis (Figure 3) revealed that the large β-grains preserved during hot rolling have an irregular predominantly elongated shape with slip bands

inside. A significant fraction of β-grains appears heavily fragmented, presumably due to the development of dynamic recrystallization processes during deformation. This partially recrystallized structure is typical of semi-finished products obtained during hot deformation in a single-phase field [44].

Microindentation testing provided the following values of physical-mechanical properties in the hot-rolled alloy: Vickers microhardness—215 HV, contact elastic modulus—70 GPa. The microhardness value of the alloy in the hot-rolled β-state is relatively low. Additionally, the contact elastic modulus is approximately 1.5 times lower than that of CP-titanium and the Ti-6Al-4V ELI type alloy (103–110 GPa [2]). A similar elastic modulus was reported in [45] for a biocompatible β-alloy of the Ti-Nb-Zr-Ta system.

SEM microstructure of Ti39Nb7Zr after RF was obtained and is presented in Figure 4.

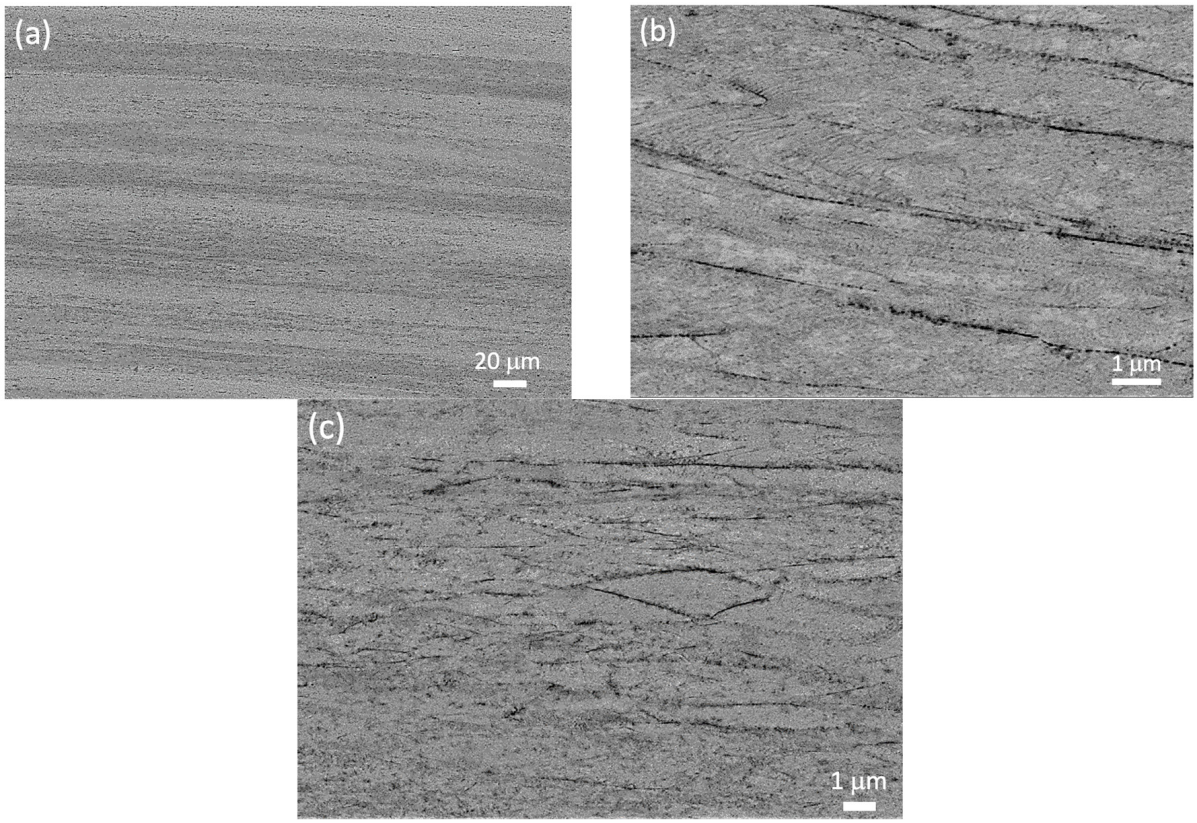

Figure 4. SEM microstructure of Ti39Nb7Zr after rotary forging: (**a**) β-grains along the rod axis, (**b**,**c**) areas with thinner boundaries typical for sub-grains.

The microstructure analysis at low magnifications revealed the processes of elongation of β-grains along the rod axis and their flattening in the perpendicular direction occurring during RF (Figure 4a). The sizes of β-grains ranged from 0.5 to 5 µm (Figure 4b). Upon examination of the structure at high magnifications, slip bands within the β-grains were observed (Figure 4b), the presence of areas with thinner boundaries typical for subgrains (Figure 4b,c), as well as relatively small β-grains, which apparently formed during dynamic recrystallization during RF (Figure 4c). Dark spots within the β-grain body created an inhomogeneous contrast in the SEM image. The boundaries have a necklace morphology (Figure 4b). Both of these effects may be associated with the presence of a second phase.

TEM analysis was performed for a more detailed analysis of the microstructure and phase composition of the alloy after RF (Figure 5). The interpretation of the electron diffraction pattern is presented in Table 3.

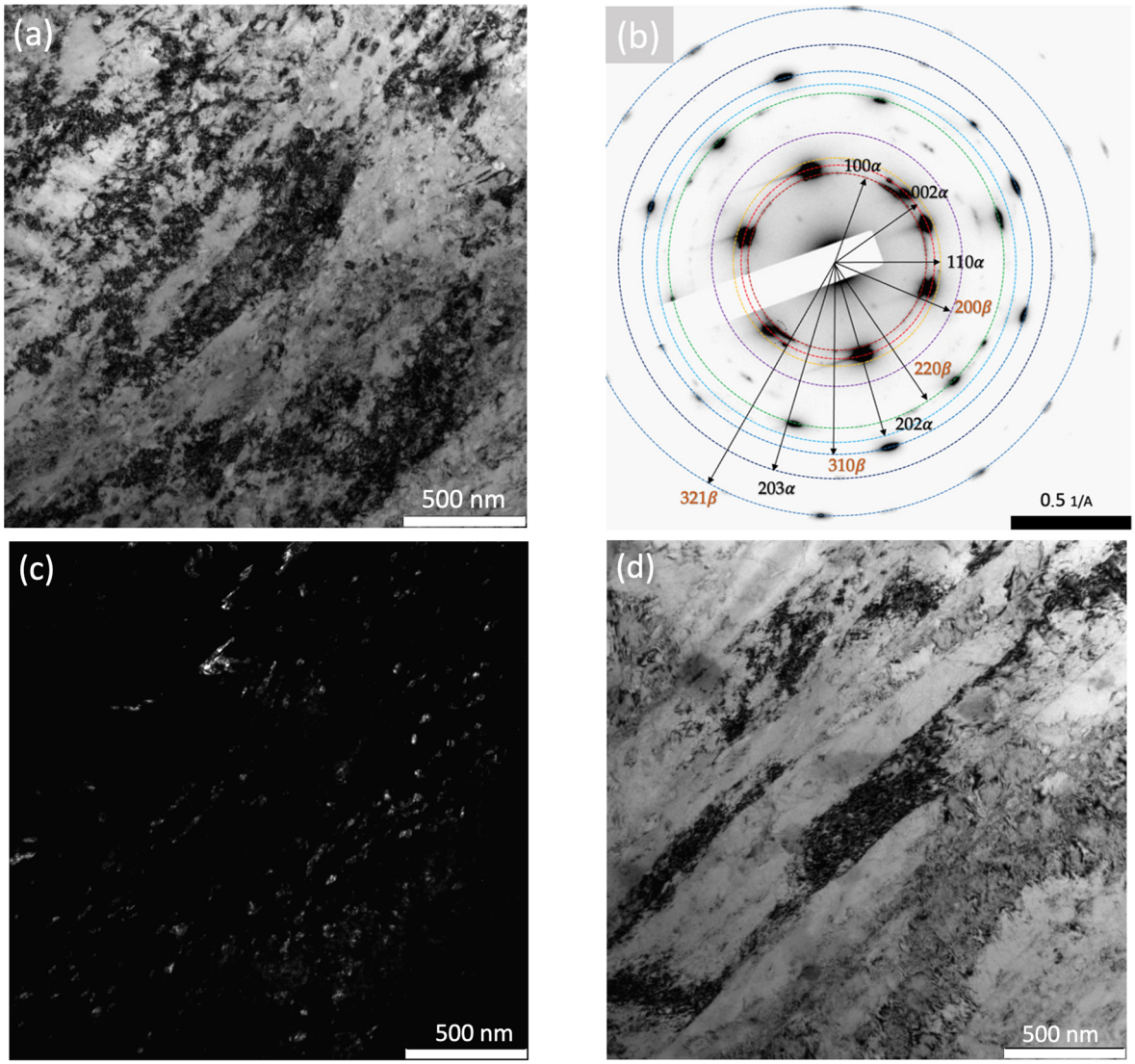

Figure 5. TEM microstructure of Ti39Nb7Zr after RF: (**a**,**d**) bright field images, (**b**) electron diffraction pattern from (**a**); (**c**) dark field in the <100>α reflection.

Table 3. Specification for electron diffraction pattern (Figure 5b) of the Ti-39Nb-7Zr alloy.

Phase	d_{exp}	h	k	l	d_{ref}	d_{comp}
α	2.564	1	0	0	2.558	-
α	2.353	0	0	2	2.341	-
α	2.247	1	1	0	2.244	-
β	1.667	2	0	0	-	1.648
β	1.177	2	2	0	-	1.165
α	1.124	2	0	2	1.119	-
β	1.053	3	1	0	-	1.042
α	0.991	2	0	3	0.987	-
β	0.885	3	2	1	-	0.881

TEM data analysis showed an increased density of dislocations inside the elongated β-grains formed during RF, these appeared as both individual clusters and an imperfect substructure (Figure 5a,d). Nanoscale (10–30 nm) second-phase precipitates, predominantly oriented along the grain elongation direction, were observed at the boundaries and within the grain body. These precipitates were formed during RF at 450 °C, either during preheating or intermediate heating operations, as there is no second phase in the initial

hot-deformed state. Computational analysis of electron diffraction patterns revealed that the precipitates consist of α-phase with an HCP lattice. The formation of the α-phase during the decomposition of the metastable β-solid solution at 450 °C in another biocompatible β-alloy, Ti-29Nb-13Ta-4.6Zr, was previously observed in [46].

An increase in the dislocation density in the provided TEM images is evidenced by the diffraction contrast. The accumulation of dislocations results in characteristic dark areas in the TEM images obtained from the foil in the reflecting spatial position. However, it is not possible to clearly resolve separate dislocations due to the overlap of elastic fields around individual dislocations. Joint analysis of XRD and SEM data after hot rolling (Figure 3) and SEM, TEM, and XRD after RF (Figures 4–6) points to an increase in dislocation density after RF.

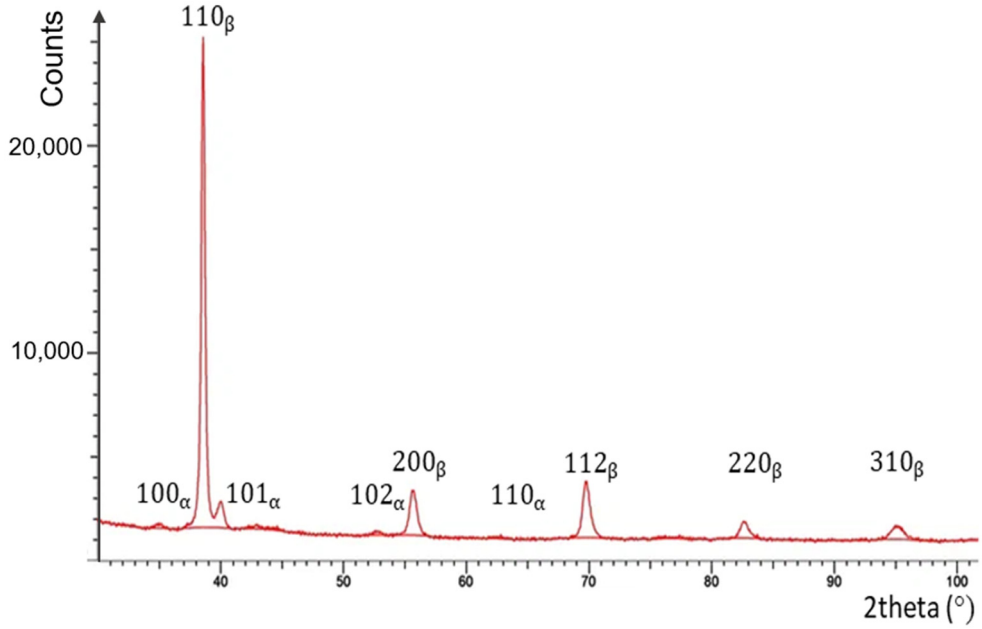

Figure 6. Diffraction pattern of Ti39Nb7Zr after rotary forging.

In this case, the Williamson–Hall method [47] was used to estimate the increase in dislocation density after RF compared to the hot-rolled state. This method relies on estimating the broadening of the β-phase XRD peaks. By conducting computations using this method, the dislocation density in the alloy is approximately estimated to be 10^9 [1/cm^2] in the hot-rolled state, while it is approximately equal to 1.6×10^{10} [1/cm^2] after RF. Thus, there is approximately a 16-fold increase compared to the hot-rolled state.

The increased dislocation density and nanosized α-particles in the β-matrix after forging led to changes in the diffraction pattern (Figure 6) and an increase in the elastic modulus (76 GPa) and microhardness (280 HV).

The peaks of the α-phase become visible, and the peaks of the β-solid solution broaden in the diffraction pattern due to elastic distortions caused by the increase in dislocation density. The calculations of the α and β-phase lattice parameters yielded the following values: a_α = 0.29532 nm, c_α = 0.46982 nm, c/a = 1.5909, a_β = 0.3292 nm. The obtained values of the β-phase lattice spacing after RF are comparable to those obtained in the hot-rolled state (0.3296 nm). The parameters of the α-phase are higher than those for pure titanium (a_α = 0.29503 nm, c_α = 0.46831 nm, c/a = 1.5873 [48]). This is typical of titanium alloys alloyed with Zr [49], implying that Nb within the solubility in the α-phase almost has no influence on its lattice parameters [50]. The approximate relationship between β-(97%) and α-phases (3%) after RF was calculated using Rietveld refinement of XRD data.

Ti39Nb7Zr is characterized by an excellent ductility of 22% in the hot-rolled state. However, it exhibits a rather poor strength of 560 MPa as obtained from the tensile engineering stress–strain curve (Figure 7). The yield strength of 860 MPa, typical of the Ti-6Al-4V

ELI alloy, is considered the gold standard for titanium implants. After RF, Ti39Nb7Zr almost reaches this strength level and exhibits the following mechanical properties: YS $\geq$ 785 MPa, UTS $\geq$ 830 MPa, EL $\geq$ 11%, RA $\geq$ 65.5%. For both processing methods, the engineering stress–strain curves of Ti39Nb7Zr show weak strain hardening at the uniform deformation stage, typical of β-titanium alloys. The strengthening of the alloy after RF resulted in a 35% decrease in ductility. There are at least two reasons why the elongation after RF is less than after the hot rolling. Firstly, due to the lower deformation temperature of 450 °C during RF compared to hot rolling in the β-region at a temperature above 600 °C. Therefore, the processes of dynamic recrystallization are more fully developed in the hot-rolled alloy, resulting in a lower dislocation density compared to RF. Secondly, nano-sized precipitates of α-phase are found in the alloy after RF; these are absent in the hot-rolled state with single phase β-structure. The presence of these precipitates additionally complicates the process of dislocations gliding during plastic deformation and, along with the higher dislocation density, contributes to the lower elongation during tensile testing.

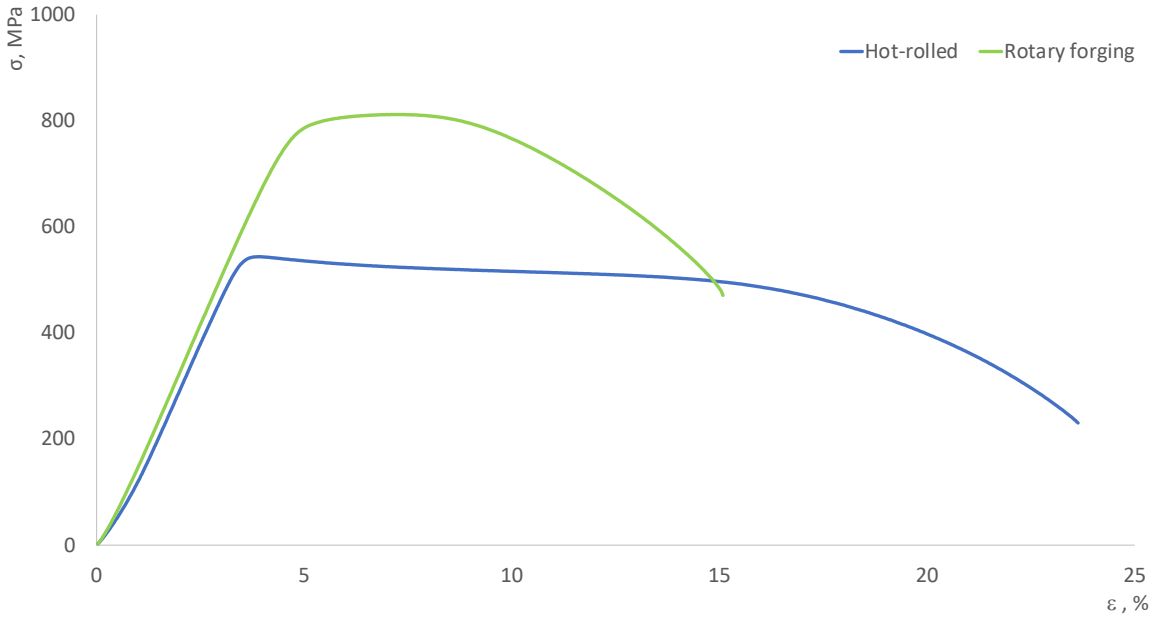

Figure 7. Engineering stress–strain curve for Ti39Nb7Zr after hot rolling and RF.

The properties obtained for the alloy after RF fall within the characteristic range for medical (α+β)-alloy Ti-6Al-4V ELI in the annealed state [51]. However, Ti39Nb7Zr does not contain chemical elements with limited biocompatibility and is characterized by an elastic modulus 1.5 times lower than that of Ti-6Al-4V ELI.

The results of the thermal stability assessment of Ti39Nb7Zr after RF, under heating to temperatures of 600 to 700 °C, combined with the determination of thermophysical properties (specific heat capacity, dynamic modulus of elasticity, thermal conductivity), are demonstrated in Figure 8.

The analysis of DTA and DMA data (Figure 8a,b) revealed minor changes in the temperature dependencies upon heating to 400–450 °C: an increase in the modulus of elasticity by 2 GPa and a decrease in specific heat capacity by 30 J/kg*K. At higher heating temperatures, a drop in the modulus of elasticity by 10 GPa in the range of 400–600 °C takes place as well as a peak appears on the specific heat capacity curve in the same temperature range. This effect, judging by the calculated β_{tr} value of the alloy (Table 1), is associated with the reverse α+β→β transformation. Thus, the dissolution of the higher modulus α-phase into the β-solid solution at heating temperatures above 400–450 °C leads to a sharp decrease in the modulus of elasticity in this range. It is worth noting that the formation of the α-phase during rotary forging, which has a higher modulus of elasticity than the β-solid

solution, contributes to the increase in the modulus of elasticity up to 76 GPa compared to the initial hot-rolled state of 70 GPa.

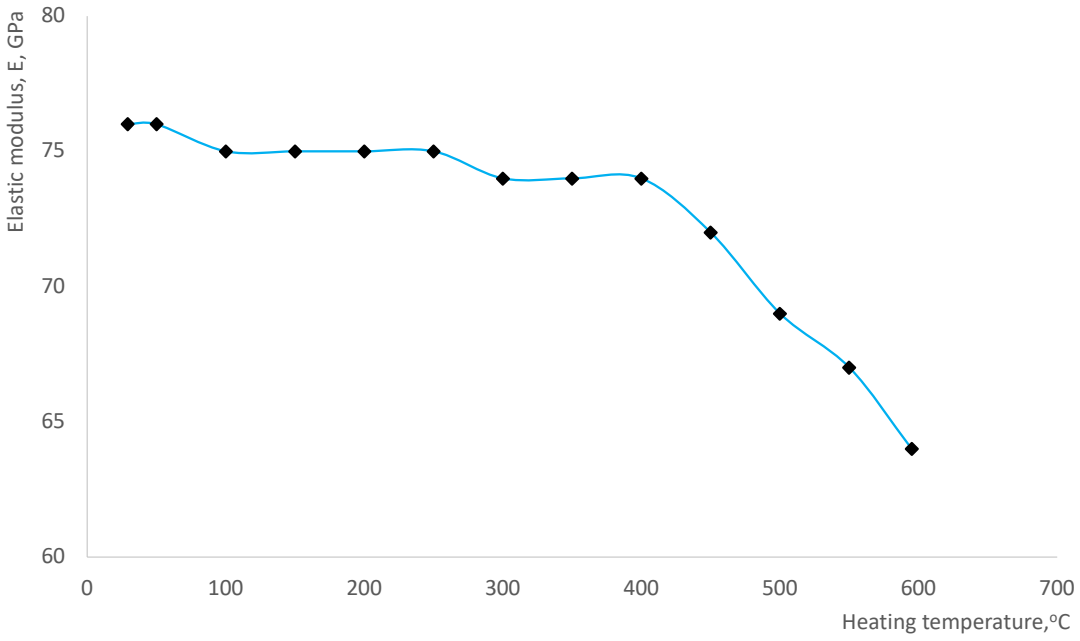

(**a**)

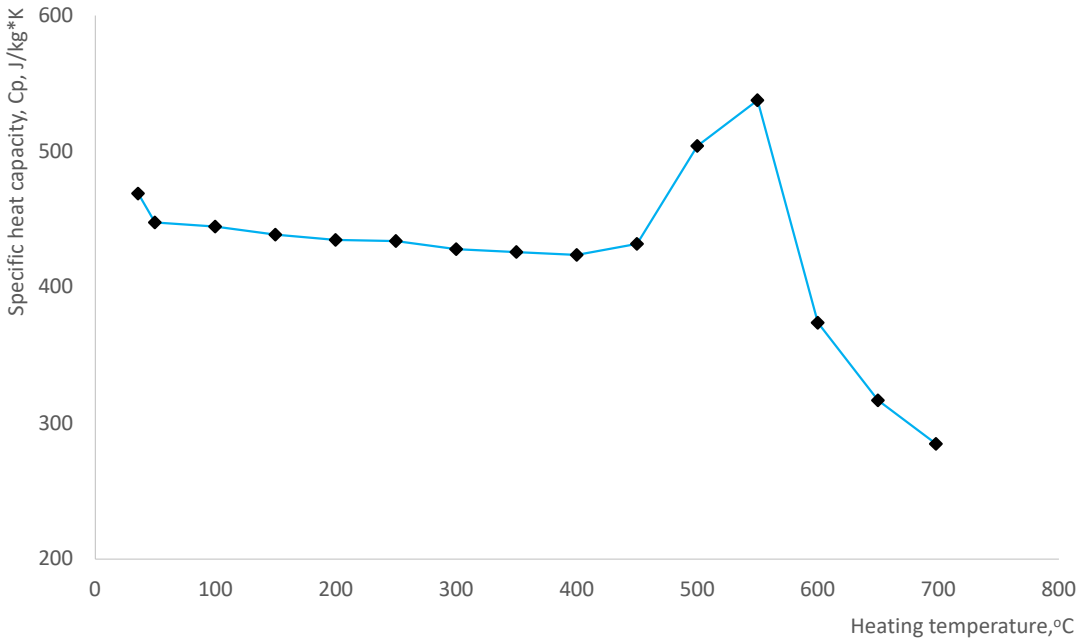

(**b**)

Figure 8. *Cont.*

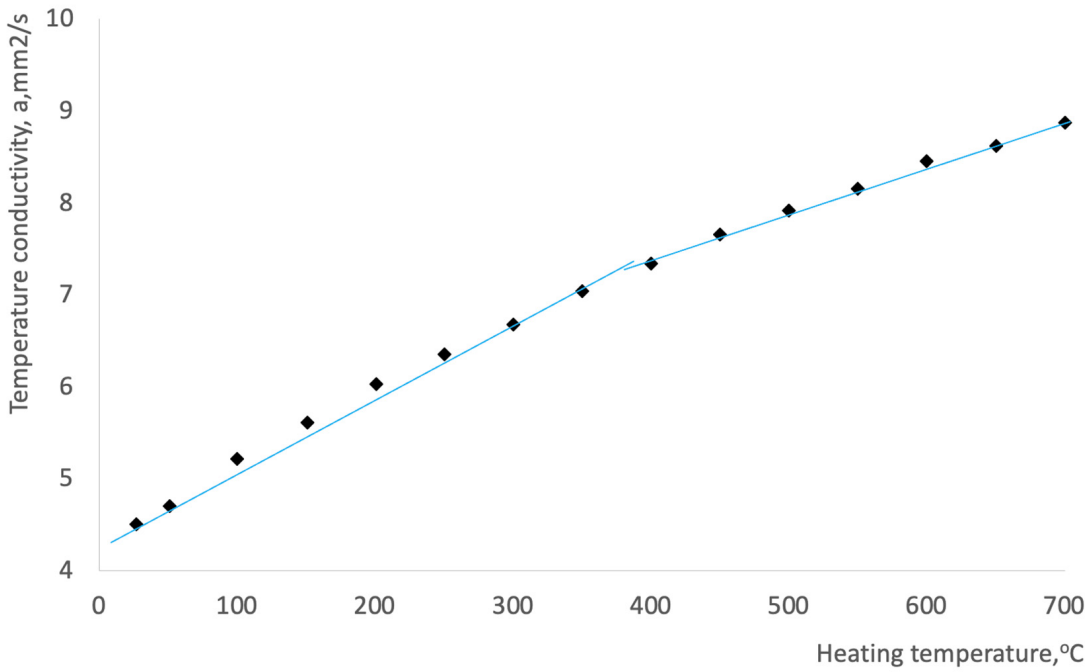

(**c**)

Figure 8. Temperature dependences of the dynamic modulus of elasticity (**a**), specific heat capacity (**b**), and thermal conductivity (**c**) during heating of the Ti39Nb7Zr alloy after RF.

Figure 8c illustrates a characteristic bottom-up dependency of thermal conductivity with increasing heating temperature. A similar trend in thermal conductivity with temperature was observed in the biocompatible β-alloy Ti-45Nb with an ultrafine grain structure in [52]. In this study, the rate of increase, i.e., the slope angle of the conductivity vs. temperature curve, decreases above 450 °C. We attribute this effect to the realization of reverse α+β→β-transformation. The dissolution of the α-phase into the β-solid solution during the transformation should lead to a decrease in the concentration of alloying elements (Nb and Zr) in the β-phase, which have a higher thermal conductivity than Ti [53].

The obtained temperature dependencies of thermophysical properties indicate that the alloy exhibits good thermal stability after RF up to heating temperatures of 450 °C. Beyond this point, it loses stability due to the development of the polymorphic α+β→β-phase transformation.

4. Conclusions

1. The hot-rolled biocompatible alloy Ti39Nb7Zr, in a single-phase β-state, exhibits a microhardness of 215 HV and a contact modulus of elasticity of 70 GPa, along with a yield strength of 565 MPa, an elongation of 22%, and a reduction area of 71%.
2. After multi-pass rotary forging at 450 °C, the microstructure of the alloy is characterized by elongated β-grains displaying a<110>-fiber texture along the rod axis. These grains are characterized by an increased dislocation density and a 500 nm subgrain structure along with nanoscale (10–20 nm) α-precipitates in the body and along the boundaries of β-grains.
3. The biocompatible alloy Ti39Nb7Zr, after RF, demonstrates a well-balanced combination of mechanical properties (YS ≥ 785 MPa, UTS ≥ 830 MPa, EL ≥ 11%, RA ≥ 65.5%) compared to the widely used medical alloy Ti-6Al-4V ELI. Moreover, Ti39Nb7Zr lacks elements with limited biocompatibility, and its modulus of elasticity (76 GPa) is 1.5 times lower than that of Ti-6Al-4V ELI, commonly used for medical implants.
4. The nature of changes in physical properties (modulus of elasticity, specific heat capacity, thermal conductivity) of Ti39Nb7Zr during heating at temperatures in the

range of 600–700 °C after RF is discussed. The satisfactory thermal stability in the RF state at heating temperatures of 400–450 °C was demonstrated. Heating of Ti39Nb7Zr above 400–450 °C after RF activates the reverse polymorphic α+β→β-phase transformation process.

Taking into account the obtained level of mechanical properties, good thermal stability, and increased biocompatibility of this alloy the rotation forging of the Ti39Nb7Zr alloy can be recommended for manufacturing the rods that can be employed as semi-products for medical bone implants.

Author Contributions: Conceptualization, S.S. and A.K.; Methodology, R.K., V.A. and V.Y.; Validation, R.K.; Formal analysis, A.I.; Investigation, G.M.; Resources, V.Y. and A.K.; Writing—original draft, A.I. and S.S.; Writing—review & editing, V.K. and V.A.; Visualization, G.M.; Supervision, V.K. All authors have read and agreed to the published version of the manuscript.

Funding: The study was financially supported by the Ministry of Science and Higher Education of the Russian Federation under the Development Program of the Ural Federal University named after the First President of Russia B.N. Yeltsin in accordance with the Strategic Academic Leadership Program "Priority-2030".

Data Availability Statement: The raw data supporting the conclusions of this article will be made available by the authors on request.

Conflicts of Interest: The authors declare no conflict of interest.

References

1. Geetha, M.; Singh, A.K.; Asokamani, R.; Gogia, A.K. Ti based biomaterials, the ultimate choice for orthopaedic implants—A review. *Prog. Mater. Sci.* **2009**, *54*, 397–425. [CrossRef]
2. Li, Y.; Yang, C.; Zhao, H.; Qu, S.; Li, X.; Li, Y. New Developments of Ti-Based Alloys for Biomedical Applications. *Materials* **2014**, *7*, 1709–1800. [CrossRef] [PubMed]
3. Niinomi, M. Design and development of metallic biomaterials with biological and mechanical biocompatibility. *J. Biomed. Mater. Res. Part A* **2019**, *107*, 944–954. [CrossRef] [PubMed]
4. Sarraf, M.; Ghomi, E.R.; Alipour, S.; Ramakrishna, S.; Sukiman, N.L. A state-of-the-art review of the fabrication and characteristics of titanium and its alloys for biomedical applications (Review). *Bio-Des. Manuf.* **2022**, *5*, 371–395. [CrossRef] [PubMed]
5. Marin, E.; Lanzutti, A. Biomedical Applications of Titanium Alloys: A Comprehensive Review. *Materials* **2024**, *17*, 114. [CrossRef] [PubMed]
6. Elias, C.N.; Lima, J.H.C.; Valiev, R.; Meyers, M.A. Biomedical applications of titanium and its alloys. *J. Miner. Met. Mater. Soc.* **2008**, *60*, 46–49. [CrossRef]
7. Banerjee, D.; Williams, J.C. Perspectives on titanium science and technology. *Acta Mater.* **2013**, *61*, 844–879. [CrossRef]
8. Kaur, M.; Singh, K. Review on titanium and titanium based alloys as biomaterials for orthopaedic applications. *Mater. Sci. Eng. C* **2019**, *102*, 844–862. [CrossRef] [PubMed]
9. Straumal, B.B.; Gornakova, A.S.; Kilmametov, A.R.; Rabkin, E.; Anisimova, N.Y.; Kiselevskiy, M.V. β-Ti-Based Alloys for Medical Applications. *Russ. J. Non-Ferr. Met.* **2021**, *62*, 54–63. [CrossRef]
10. Bahl, S.; Suwas, S.; Chatterjee, K. Comprehensive review on alloy design, processing, and performance of β Titanium alloys as biomedical materials. *Int. Mater Rev.* **2021**, *66*, 114–139. [CrossRef]
11. Sidhu, S.S.; Singh, H.; Gepreel, M.A.-H. A Review on Alloy Design, Biological Response, and Strengthening of β-Titanium Alloys as Biomaterials. *Mater. Sci. Eng. C Mater. Biol. Appl.* **2021**, *121*, 111661. [CrossRef] [PubMed]
12. Senopati, G.; Rahman Rashid, R.A.; Kartika, I.; Palanisamy, S. Recent Development of Low-Cost β-Ti Alloys for Biomedical Applications: A Review. *Metals* **2023**, *13*, 194. [CrossRef]
13. Lario, J.; Vicente, Á.; Amigó, V. Evolution of the Microstructure and Mechanical Properties of a Ti35Nb2Sn Alloy Post-Processed by Hot Isostatic Pressing for Biomedical Applications. *Metals* **2021**, *11*, 1027. [CrossRef]
14. Emsley, J. *Elements*; Mir: Moscow, Russia, 1993; p. 256.
15. Miracle, D.B.; Senkov, O.N. A critical review of high entropy alloys and related concepts. *Acta Mater.* **2017**, *122*, 448–511. [CrossRef]
16. Zhang, T.; Ou, P.; Ruan, J.; Yang, H. Nb-Ti-Zr alloys for orthopedic implants. *J. Biomater. Appl.* **2021**, *35*, 1284–1293. [CrossRef]
17. Illarionov, A.G.; Grib, S.V.; Yurovskikh, A.S. Scientific approaches to the development of titanium-based alloys for medical implants. *Solid State Phenom.* **2020**, *299*, 462–467. [CrossRef]
18. Valiev, R.Z.; Aleksandrov, I.V. *Volumetric Nanostructured Metallic Materials Obtaining, Structure and Properties: [Monograph]*; Academkniga: Moscow, Russia, 2007.

19. Yu, A.; Eroshenko, Y.P.; Sharkeyev, I.A.; Glukhov, P.V.; Uvarkin, A.M.; Mayrambekova, A.I. Tolmachev Influence of the size of structural elements and phase state on the mechanical properties of binary alloys of Ti-Nb and Zr-Nb systems. *Izv. Vyss. Vyskikh Uchebnykh Obraz. Fiz.* **2018**, *61*, 136–143.
20. Zayed, E.M.; Shazly, M.; El-Sabbagh, A.; El-Mahallawy, N.A. Review article Deformation behavior and properties of severe plastic deformation techniques for bulk materials: A review. *Heliyon* **2023**, *9*, e16700. [CrossRef]
21. Edalati, K.; Bachmaier, A.; Beloshenko, V.A.; Beygelzimer, Y.; Blank, V.D.; Botta, W.J.; Bryła, K.; Čížek, J.; Divinski, S.; Enikeev, N.A.; et al. Nanomaterials by severe plastic deformation: Review of historical developments and recent advances. *Mater. Res. Lett.* **2022**, *10*, 163–256. [CrossRef]
22. Markushev, M.V. On the efficiency of some methods of intense plastic deformation intended for obtaining bulk nanostructured materials. *Lett. Mater.* **2011**, *1*, 36–42. [CrossRef]
23. Mao, Q.; Liu, Y.; Zhao, Y. Review A review on mechanical properties and microstructure of ultrafine grained metals and alloys processed by rotary swaging. *J. Alloys Compd.* **2022**, *896*, 163122. [CrossRef]
24. Raab, G.I.; Aleshin, G.N.; Fakhretdinova, E.I.; Raab, A.G.; Asfandiarov, R.N.; Aksenov, D.A.; Kodirov, I.S. Prospects for the development of new experimental and commercial methods of severe plastic deformation. *MaTeD* **2019**, *1*, 48–57.
25. Moiseenkov, V.V.; Sevalnev, G.S.; Volkov, R.B.; Dulnev, K.V.; Levin, E.A. Application of the rotary forging method to produce rods from high-nitrogen steel VNS-78. *Aviat. Mater. Technol.* **2022**, *4*, 3–15. [CrossRef]
26. Dedyulina, O.K.; Salishchev, G.A. Formation of ultrafine-grained structure in medium carbon steel 40ХГНМ by rotary forging and its influence on mechanical properties. *Fundam. Res.* **2013**, *1*, 701–706.
27. Chuvil'deev, V.N.; Kopylov, V.I.; Nokhrin, A.V.; Bakhmet'ev, A.M.; Tryaev, P.V.; Tabachkova, N.Y.; Chegurov, M.K.; Kozlova, N.A.; Mikhailov, A.S.; Ershova, A.V.; et al. Enhancement of the Strength and the Corrosion Resistance of a PT-7M Titanium Alloy Using Rotary Forging. *Russ. Metall. (Met.)* **2021**, *2021*, 600–610. [CrossRef]
28. Naydenkin, E.V.; Mishin, I.P.; Zabudchenko a, O.V.; Lykova, O.N.; Manisheva, A.I. Structural-phase state and mechanical properties of β titanium alloy produced by rotary swaging with subsequent aging. *J. Alloys Compd.* **2023**, *935*, 167973. [CrossRef]
29. Rogachev, S.O.; Andreev, V.A.; Gorshenkov, M.V.; Ten, D.V.; Kuznetsova, A.S.; Scherbakov, A.B. Improvement of strength characteristics of Zr-2.5% Nb alloy by rotary forging. *Phys. Met. Metall.* **2022**, *123*, 1002–1008.
30. Freitas Rodrigues, P.; Teixeira, R.S.; Le Sénéchal, N.V.; Braz Fernandes, F.M.; Paula, A.S. The Influence of the Soaking Temperature Rotary Forging and Solution Heat Treatment on the Structural and Mechanical Behavior in Ni-Rich NiTi Alloy. *Materials* **2021**, *15*, 63. [CrossRef] [PubMed]
31. Ma, X.-Q.; Yu, Z.-T.; Liu, H.-Y.; Cheng, J.; Niu, J.-L.; Yu, S. Microstructures and Properties of Ti-25Nb-15Zr Alloy for Spectacle Frame. *Key Eng. Mater.* **2017**, *727*, 191–195. [CrossRef]
32. Bartha, K.; Stráský, J.; Veverková, A.; Veselý, J.; Čížek, J.; Málek, J.; Polyakova, V.; Semenova, I.; Janěcek, M. Phase Transformations upon Ageing in Ti15Mo Alloy Subjected to Two Different Deformation Methods. *Metals* **2021**, *11*, 1230. [CrossRef]
33. Wang, Q.; Dong, C.; Liaw, P.K. Structural Stabilities of β-Ti Alloys Studied Using a New Mo Equivalent Derived from [β/(α + β)] Phase-Boundary Slopes. *Metall. Mater. Trans. A* **2015**, *46*, 3440–3447. [CrossRef]
34. Abdel-Hady, M.; Hinoshita, K.; Morinaga, M. General approach to phase stability and elastic properties of β-type Ti-alloys using electronic parameters. *Scripta Mater.* **2006**, *55*, 477–480. [CrossRef]
35. Abdel-Hady, M.; Fuwa, H.; Hinoshita, K.; Kimura, H.; Shinzato, Y.; Morinaga, M. Phase stability change with Zr content in β-type Ti–Nb alloys. *Scr. Mater.* **2007**, *57*, 1000–1003. [CrossRef]
36. Miyazaki, S. My experience with Ti–Ni-based and Ti-based shape memory alloys. *Shap. Mem. Superelasticity* **2017**, *3*, 279–314. [CrossRef]
37. Hao, Y.L.; Li, S.J.; Prima, F.; Yang, R. Controlling reversible martensitic transformation in titanium alloys with high strength and low elastic modulus. *Scr. Mater.* **2012**, *67*, 487–490. [CrossRef]
38. Korenev, A.; Illarionov, A.G. Influence of cold deformation on structure, texture, elastic and microrodurometric properties of biocompatible beta-titanium alloys based on Ti-Nb-Zr system. *FMM* **2023**, *124*, 492–499.
39. *ASTM E1269*; Standard Test Method for Determining Specific Heat Capacity by Differential Scanning Calorimetry. ASTM: West Conshohocken, PA, USA, 2011.
40. Parker, W.J.; Jenkins, R.J.; Butler, C.P.; Abbott, G.L. Flash Method of Determining Thermal Diffusivity, Heat Capacity, and Thermal Conductivity. *J. Appl. Phys.* **1961**, *32*, 1679–1684. [CrossRef]
41. Polukhin, P.I.; Gorelik, S.S.; Vorontsov, V.K. *Physical Bases of Plastic Deformation*; Metallurgy: Moscow, Russia, 1982; p. 584.
42. Levinger, B.W. Lattice Parameter of Beta Titanium at Room Temperature. *Trans. AIME J. Met.* **1953**, *5*, 195. [CrossRef]
43. Khrunyk, Y.Y.; Ehnert, S.; Grib, S.V.; Illarionov, A.G.; Stepanov, S.I.; Popov, A.A.; Ryzhkov, M.A.; Belikov, S.V.; Xu, Z.; Rupp, F.; et al. Synthesis and Characterization of a Novel Biocompatible Alloy, Ti-Nb-Zr-Ta-Sn. *Int. J. Mol. Sci.* **2021**, *22*, 10611. [CrossRef]
44. Grachev, S.V.; Rodaz, V.R.; Bogatov, A.A.; Shveikin, V.P. *Physical Metallurgy*; UGTU-UPI: Ekaterinburg, Russia, 2001; p. 534.
45. Hynowska, A.; Pellicer, E.; Fornell, J.; González, S.; van Steenberge, N.; Suriñach, S.; Gebert, A.; Calin, M.; Eckert, J.; Rodó, M.D.; et al. Nanostructured β-phase Ti-31.0Fe-9.0Sn and sub-μm structured Ti-39.3Nb-13.3Zr-10.7Ta alloys for biomedical applications: Microstructure benefits on the mechanical and corrosion performances. *Mater. Sci. Eng. C* **2012**, *32*, 2418–2425. [CrossRef]
46. Hao, Y.L.; Niinomy, N.; Kuroda, D.; Fukunaga, K.; Zhou, Y.L.; Yang, R.; Suzuki, A. Aging Response of the Young's Modulus and Mechanical Properties of Ti-29Nb-13Ta-4.6Zr for Biomedical Applications. *Metall. Mater. Trans. A* **2003**, *34*, 1007–1012. [CrossRef]

47. Ivanov, I.; Safarova, D.; Bataeva, Z.; Bataev, I. Comparison of approaches based on the Williamson-Hall method for analyzing the structure of the high-entropy alloy Al0.3CoCrFeNi after cold plastic deformation. *Met. Process.* **2022**, *24*, 90–102. [CrossRef]
48. Kolachev, B.A.; Livanov, V.I.; Elagin, V.A. *Metallology and Heat Treatment of Non-Ferrous Metals and Alloys*; Metallurgy: Moscow, Russia, 1999; 416p.
49. Zwicker, U. *Titanium and Its Alloys*; Metallurgy: Moscow, Russia, 1979; 512p.
50. Moffat, D.L.; Larbalestier, D.C. The Competition between Martensite and Omega in Quenched Ti-Nb Alloys. *Metall. Trans. A* **1988**, *19*, 1677–1686. [CrossRef]
51. ASM International. *Metals Handbook, Properties and Selection: Nonferrous Alloys and Special-Purpose Metals*, 10th ed.; ASM International: Almere, The Netherlands, 1990; Volume 2.
52. Legostaeva, E.V.; Sharkeyev, Y.P.; Belyavskaya, O.A.; Vavilov, V.P.; Skripnyak, V.A.; Zhilyakov, A.Y.; Kuznetsov, V.P.; Eroshenko, A.Y. Influence of ultrafine-grained state on thermophysical properties of alloys Zr—1 wt.% Nb and Ti—45 wt.% Nb and processes of dissipation and accumulation of energy during deformation// IZVESTIJA Vysshee HIGH SCHOOLS. *Physics* **2020**, *63*, 28–35.
53. Gorbatov, V.I.; Polev, V.F.; Pilyugin, V.P.; Korshunov, I.G.; Smirnov, A.L.; Taluts, S.G.; Brytkov, D.A. Temperature conductivity of submicro- and nanocrystalline niobium, titanium, and zirconium at high temperatures. *Thermophys. High Temp.* **2013**, *51*, 539–542.